# **LinPrim: Linear Primitives for Differentiable Volumetric Rendering**

### Nicolas von Lützow

Technical University of Munich nicolas.von-luetzow@tum.de

# Matthias Nießner

Technical University of Munich niessner@tum.de



Figure 1: We present LinPrim, a new take on novel view synthesis, that leverages linear primitives - octahedra and tetrahedra - for differentiable volumetric rendering in order to facilitate 3D scene reconstruction. To this end, we propose a differentiable rendering pipeline in conjunction with a real-time capable rasterizer tailored to such primitives, thus achieving interactive frame rates for novel-view rendering and showcasing the potential of polyhedral primitives in NVS workflows.

#### Abstract

Volumetric rendering has become central to modern novel view synthesis methods, which use differentiable rendering to optimize 3D scene representations directly from observed views. While many recent works build on NeRF [18] or 3D Gaussians [13], we explore an alternative volumetric scene representation. More specifically, we introduce two new scene representations based on *linear* primitives—octahedra and tetrahedra—both of which define homogeneous volumes bounded by triangular faces. To optimize these primitives, we present a differentiable rasterizer that runs efficiently on GPUs, allowing end-to-end gradient-based optimization while maintaining real-time rendering capabilities. Through experiments on real-world datasets, we demonstrate comparable performance to state-of-the-art volumetric methods while requiring fewer primitives to achieve similar reconstruction fidelity. Our findings deepen the understanding of 3D representations by providing insights into the fidelity and performance characteristics of transparent polyhedra and suggest that adopting novel primitives can expand the available design space. <sup>1</sup>

https://nicolasvonluetzow.github.io/LinPrim/

# 1 Introduction

Novel View Synthesis (NVS) enables a holistic understanding of 3D scenes given only 2D observations. This capability is essential to a range of applications, including VR/AR, robotics, and autonomous driving. The success of state-of-the-art NVS approaches depends heavily on the chosen scene representations and the processes used to render them. In addition to visual quality, the representations have inherent characteristics that largely impact the ability to work with the reconstructed scenes in downstream applications. Explicit representations have proven particularly desirable due to their easily interpretable and manipulable structures.

Approaches in NVS utilize a wide range of scene representations that differ significantly from the conventional triangle-mesh-based pipelines used in most 3D applications. While triangle meshes are central to standard 3D content creation, their direct optimization in NVS tasks remains challenging [21, 6]. Instead, it is essential to explore the extensive design space of possible representations to assess how they impact fidelity, performance and stability in NVS settings.

The strongest visual quality in NVS applications is currently achieved by approaches relying on *Neural Radiance Fields* (NeRF) [18, 3, 1, 2]. Although the results are impressive, NeRFs encode an implicit function, making them suboptimal for downstream applications. For instance, editing or scene animation require elements to be easily identified, accessed, or manipulated, which is inherently difficult with NeRF representations [31, 22]. Additionally, the corresponding volumetric rendering process is computationally expensive, often making real-time applications infeasible. More recently, *3D Gaussian Splatting* (3DGS) [13] introduced a real-time capable, explicit representation that also achieves strong visual performance. The 3DGS representation consists of 3D Gaussian kernels, which are optimized on known views to adjust their position and features. As evidenced by the large body of derivative works relying on 3DGS [30, 12, 17, 5, 25], the explicit nature of the representation simplifies integration into other pipelines and settings.

Motivated by the scientific curiosity of how simple, bounded primitives can be used to reconstruct high-fidelity real-world scenes, we explore an alternative to 3DGS by employing transparent polyhedra as our scene representation. Specifically, we introduce two novel scene representations based on octahedron and tetrahedron primitives. Each primitive is characterized by a compact set of features that describe its position, vertices, opacity, and view-dependent appearance. These primitives are bounded by triangular faces and of homogeneous density, which makes them an intuitive representation that can be easily understood and modified.

We build on the 3DGS pipeline to accommodate the new primitives. Our method first constructs polyhedra from a concise set of features in a fully differentiable manner. During rendering, we then rely on simple ray-triangle intersections to determine the opacity of each primitive and successively blend them. As a result, we can backpropagate image-space errors through the intersection calculations to distribute gradients onto the geometric features of each polyhedron. The optimization pipeline remains analogous to 3DGS, yet the bounded, triangular geometry of our primitives expands the applicability of differentiable rendering pipelines. Finally, we analyze the photometric reconstruction quality and performance of our approaches on real-world scenes. We are able to show comparable results while retaining real-time rendering speeds.

To sum up, our contributions are as follows:

- We introduce two novel scene representations based on transparent octahedron and tetrahedron primitives.
- We derive gradient-based optimization processes for the representations to adjust the primitives and population based on known views.
- We demonstrate that our differentiable, GPU-based rendering pipeline is real-time capable and produces high-fidelity scene reconstructions on real-world datasets.

# 2 Related Works

**Volumetric Rendering of Radiance Fields** A major innovation in NVS has been the development of volumetric rendering approaches that represent scenes as continuous radiance fields. The seminal Neural Radiance Fields [18] demonstrated how to learn a 5D function, mapping 3D coordinates

and viewing directions to color and density, using a neural network. The rendering process used is differentiable, enabling the optimization of the representation given a known set of input views. Since its introduction, many subsequent works have improved on the initial approach. In particular, Mip-NeRF [1, 2] and Zip-NeRF [3] have drastically improved the visual quality by introducing multi-scale representations, anti-aliasing, and learned compression techniques. Instant-NGP [20] takes a different approach by accelerating both training and inference times via a multiresolution hash-based encoding strategy, allowing near real-time reconstruction and rendering.

Despite these advancements, NeRF-based methods remain primarily implicit, often resulting in comparatively high rendering and optimization costs. Their implicit nature can limit usability in downstream tasks. Since geometry and appearance are learned as continuous fields, no explicit surface representation is available by default. Using NeRF-based representations in downstream applications thus relies on specialized approaches or expensive post-processing [27, 26].

**Differentiable Point-based Rendering** Point-based rendering has traditionally been seen as an alternative to mesh-based pipelines due to its simplicity in handling geometry and varying levels of surface detail [32, 10]. More recently, differentiable point-based methods have emerged, enabling end-to-end optimization of both geometry and appearance from image supervision [23, 28, 16].

The seminal work of 3D Gaussian Splatting [13] replaces traditional point primitives with elliptical Gaussian kernels. By optimizing the position and shape of the kernels from known views, they can create an explicit 3D reconstruction from known views. Additionally, each Gaussian can be efficiently "splatted" onto the screen space, allowing for real-time rendering performance. Building on the foundation of 3D Gaussian Splatting, *Mip-Splatting* [30] tackles aliasing by controlling the maximum frequency of the splats, effectively reducing flickering and dilation artifacts. This is achieved by filtering and scaling Gaussian primitives to better match the level of detail required at different viewing distances, preventing excessively sharp or overlapping splats.

Other works replace the Gaussian distributions with other primitives to achieve improved performance. *Beyond Gaussians* [4], replaces Gaussian kernels with linear kernels to achieve sharper and more precise results in high-frequency regions. Compared to our work, however, the primitives remain elliptical and non-homogeneous in density. In contrast, *EVER* [17] uses homogeneous density ellipsoids to replace alpha-blending with an exact rendering process, which avoids popping artifacts. *3D Convex Splatting* [11] employs 3D smooth convexes, completely detaching it from the Gaussian context. Their primitives offer improved flexibility and reconstruction quality.

Although these methods offer notable improvements, we instead aim to explore novel representations that rely on simple distinct primitives. While all of the above methods introduce novel primitives or rendering processes, they share the general optimization process using known views and differentiable rendering. As such, we aim to foster innovation by exploring foundational primitives to improve the general understanding of the scene representations used in NVS settings. For this, our work focuses on transparent polyhedra bounded by triangular faces, keeping compatibility with conventional geometry-processing tools while maintaining high fidelity and rendering speed.

# 3 Method

# 3.1 Linear Rendering Primitives

We introduce two representations based primarily on polyhedron primitives. For each primitive, a set of features that can accurately describe its shape needs to be defined. In our case, these include geometric parameters, position, opacity, and color.

**Octahedra.** Importantly, there is a wide range of possible octahedra of which we only model a subset. We specifically ignore cases with non-triangular faces, which are difficult to handle and can lead to unpredictable numbers of vertices and edges. Moreover, to prevent degenerate cases, we limit the degrees of freedom by restricting vertex positions to lie on the coordinate axes relative to the center. To increase expressiveness, we instead optimize a rotation quaternion for each primitive, which ensures the shape can be oriented arbitrarily in space.

We enforce symmetry by choosing a single distance to describe opposing corners. Hence, each pair of opposite vertices shares the same distance from the center, effectively reducing the complexity

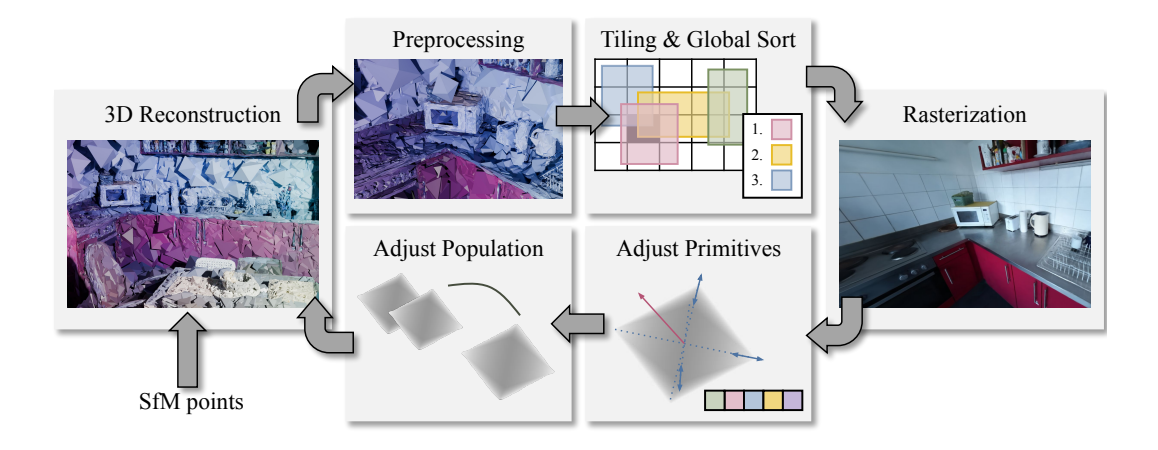


Figure 2: **Overview** of our method. Primitives are constructed from SfM points. During rendering, primitives are preprocessed according to the camera pose and sorted front-to-back. Afterwards, the list is traversed and the individual color contributions are blended for each pixel. Through comparison with a known view, the primitives' features and the population are adjusted based on gradient flow.

of shape parameters. Aside from improving stability, this ensures that the center is always the true geometric center of the octahedron, simplifying downstream tasks such as bounding volume calculations and ray space approximation.

**Tetrahedra.** Although we focus primarily on octahedra, the same principles can be extended to accommodate many types of homogeneous volumes. As a particular example, we demonstrate the usage of tetrahedron primitives to reconstruct scenes. Contrary to octahedra, even regular tetrahedra are not symmetric along all axes and thus require adjustments to the stored features. In particular, we define four basis vectors, which describe directions from the center on which corners are located. All basis vectors are equally spaced such that they can represent regular tetrahedra. We then once again optimize for the distance between the center and each corner, keeping the process largely the same. Contrary to octahedra, this means that the optimized position can differ from the geometric center of the primitive.

**Memory Requirements.** In total, omitting color, each primitive is fully described by its center, rotation, corner distances, and opacity. For octahedra, this yields 11 floats in total, matching the parameter budget of a standard Gaussian kernel. Due to the absence of symmetry in our formulation, tetrahedra require 12 floats instead.

To describe colors and their view-dependent appearance, we utilize Spherical Harmonics (SH) coefficients, following the same approach described in 3DGS. Each primitive thus also stores a set of 48 SH coefficients, which aim to capture complex reflectance properties under varying angles of illumination and view. Because each coefficient is stored as a float, this set of SH parameters accounts for the majority of the memory used per primitive—by a significant margin compared to the geometric parameters. Thus, reducing memory consumption, in practice, hinges largely on either lowering the SH degree or decreasing the total number of primitives in the scene.

# 3.2 Rendering Process

We use a two-stage rendering process, beginning with per-primitive preprocessing and followed by per-pixel rasterization. This approach enables efficient parallelization by allowing many primitives to be processed in parallel before the final compositing stage.

**Preprocessing.** During preprocessing, we construct each primitive from the aforementioned features (*i.e.* the position, distances, and rotation). Given the camera pose, we then transform the primitives

into the camera's coordinate system and calculate the view-dependent color based on the viewing direction. Afterwards, we project these primitives into the 3D affine ray space approximation introduced in EWA Splatting [32, 33]. Because small primitives are needed to achieve high-fidelity reconstructions, and because the approximation error grows with increasing distance from the center points, we found that the resulting error remains negligible while still reducing overall performance overhead. Lastly, we compute each primitive's projected bounding box in screen space to later derive the pixels from which it is visible.

**Global Sorting and Tiling.** Following preprocessing, we leverage the tiling and global sorting techniques from 3DGS to map primitives to their corresponding pixels efficiently. We tile the screen into regions and sort primitives within each tile according to approximate front-to-back order.

**Rasterization.** During rasterization, each pixel ray either intersects a given primitive twice or not at all since the introduced primitives are convex. To find intersections, we use the *Möller-Trumbore intersection algorithm* (MTIA) [19], which is fully differentiable and thus usable in our gradient-based optimization. If there are no intersections, the primitive is not visible; if there are two, the opacity depends on the distance between the intersection points. As our reconstruction is scale ambiguous, we must normalize the obtained intersection distances to ensure consistent appearance across different scene sizes. We do this by determining the smallest distance d of the primitives and then scaling all distance measurements accordingly in a manner similar to EVER [17]. *I.e.* given the opacity of a primitive  $\alpha$ , we define the density of an octahedron as:

$$\sigma(\alpha) = -\frac{\log(1 - 0.99 \cdot \alpha)}{2 \cdot \min(d_x, d_y, d_z)}.$$
(1)

**Compositing.** Finally, we aggregate the color contributions of all visible primitives via alpha blending in front-to-back order. Because we maintain a sorted list of primitives for each tile, we can stop blending once cumulative opacity reaches a predefined threshold (*i.e.* 0.999), improving performance without noticeably affecting quality. While this approach simplifies behavior when primitives overlap, the end result is a high-fidelity rendering that faithfully reproduces fine geometry while being efficient enough for real-time applications, as shown in Appendix A.

# 3.3 Anti-Aliasing

In the context of Gaussian kernels, Mip-Splatting [30] introduced two antialiasing methods for Gaussian primitives: a 3D smoothing filter and a 2D Mip filter. In conjunction, they are able to control the maximum frequency of primitives, mitigating aliasing and dilation artifacts.

We adopt their 3D smoothing strategy to limit how small primitives can become based on visibility from the training views. As a result, each primitive is visible from at least one pixel of a training view. However, applying their 2D Mip filter approach is not possible for our primitives because they rely on modifying the screen space Gaussian distribution. Instead, for each primitive, we identify vertices that lie on the bounding box used for tiling and shift them outward, parallel to the screen. This effectively enlarges the bounding box footprint and increases the minimum size at which the primitive appears. Moreover, because the fall-off within each primitive is still treated as linear, expanding the distance from the center raises the opacity along the primitive as it is evaluated over a larger extent. Conceptually, this approach acts as a coarse approximation that serves to band-limit the high frequencies that would otherwise cause visible aliasing. Although this approach is not fully mathematically equivalent to a 2D Mip filter, it captures its function and empirically mirrors its behavior. We evaluate the effectiveness of the filters in Appendix B.

# 3.4 Optimization

We employ differentiable rendering to optimize our primitives' features from known views. For this, we use the loss formulation of 3DGS [13], consisting of L1 and SSIM terms. The gradients are then optimized using ADAM [15] and backpropagated through the entire rendering pipeline, effectively distributing the updates across the primitive features.

**Rasterization Backpropagation.** As a first step, backpropagation through the blending process yields gradients with respect to each primitive's alpha and color. When these gradients are propagated

further, the alpha gradient indicates whether the primitive should be more or less transparent and, consequently, whether the intersections should move closer together or farther apart along the pixel's ray. By following the resulting intersection gradients, we can adjust each primitive's center and vertices accordingly to achieve the desired changes. This corresponds to backpropagation through the MTIA, where the intersection depth is influenced by the position of each of the corners of the triangle. In turn, the positions of the corners depend on the position of the ray space center and the offsets to it. Combining the above, by aggregating over the corners and both intersections, we can propagate gradients from alpha to the geometric features.

**Preprocessing Backpropagation.** By this point, the gradients describe the loss w.r.t. the features that were originally passed to the rasterization step. While they already describe desired changes to the position of the center and corners, they do so in ray space. As a consequence, propagation through the preprocessing first involves reversing the projection and view transformations, yielding world space gradients. The final center gradients are a combination of the propagated ray space center gradients and the impact of the position on the ray space approximation and view-dependent color. Finally, the gradient flow w.r.t. to the corners splits when undoing the rotation, onto quaternion and distance features, respectively. As our scenes are scale ambiguous, we use the maximum distance between two training cameras to approximate their size and adjust the learning rates for position and distances accordingly.

#### 3.5 Population Control

While the above optimization process can effectively optimize a set of primitives, it cannot create or remove them if required. In addition to an initialization scheme, this raises the need for additional processes to control the population of primitives. While we generally adapt the processes introduced by 3DGS, they require adjustments to accommodate the novel primitives.

**Initialization.** We initialize a primitive for each *Structure-from-Motion* (SfM) [24] point using its position and color. Every primitive is constructed with equal distance features to all corners, using the distance between the corresponding SfM point and its closest neighbor as a starting point. While Gaussian kernels are circular when initialized and thus unaffected by rotations, our kernels are not. Thus, we initialize the primitives with a uniformly random rotation quaternion to create a more homogeneous spatial coverage.

**Adaptive Population Control.** Efficient population control requires processes to prune undesired primitives and create ones that can improve fidelity. For pruning, primitives are removed if they are too transparent, too large relative to the



Figure 3: **Visualization** of our scene representation. We show all octahedra with an opacity of at least 0.25 on an optimized Mip-NeRF 360 [2] Bicycle scene reconstruction.

scene extent, or take up too much screen space of a known view. This necessitates defining the size of a primitive to determine these criteria. For octahedra, we define their size as their longest axis, *i.e.* twice the size of the longest distance. For tetrahedra, determining their largest possible depth is more involved, and we instead approximate using  $\sqrt{2}$  times the distance to the furthest corner.

Creating new primitives is realized as either cloning or splitting existing ones. For this, primitives that have large view-space positional gradients are chosen, with smaller ones being cloned and larger ones being split based on the size of the primitives, as described above, and the size of the scene. Cloning a primitive creates a new primitive with the same features but without the gradient momentum which is directly applicable to our representations.

Splitting, on the other hand, usually involves creating two new primitives with smaller sizes and placing them by sampling from the original Gaussian as a PDF. To adjust this for octahedra, since the distances are aligned with the coordinate axes and symmetric, we sample the new positions from a PDF with standard deviations set to the corresponding distance and apply rotation afterwards. This

way, primitives are more likely to spread along the longer dimensions of the octahedra. For tetrahedra, this is not trivially possible and we instead set all standard deviations to half the largest distance. A sample result of the resulting population of octahedra can be seen in Figure 3.

# 4 Experiments

We evaluate our results on Mip-NeRF 360 [2] and ScanNet++ v2 [29]. For Mip-NeRF 360, we use all 9 available scenes, while for ScanNet++, we use only the first five NVS scenes with available test views. We train and test on the official splits provided by each dataset and maintain consistent parameters across all evaluated scenes. All approaches are trained for 30k iterations.

Following prior work, we use Mip-NeRF 360 outdoor scenes at quarter resolution and indoor scenes at half resolution. For ScanNet++ scenes, we use the official toolkit to undistort the images and use them at full resolution. All approaches are trained, rendered, and evaluated at the same resolution.

While there is a large body of work offering improvements to 3DGS, we mainly focus on the original work and the changes made by Mip-Splatting, as they most closely relate to the foundational changes made by our approach. We believe that much of the recent progress made on improving 3DGS can similarly be applied to our approach to further improve quality and performance metrics.

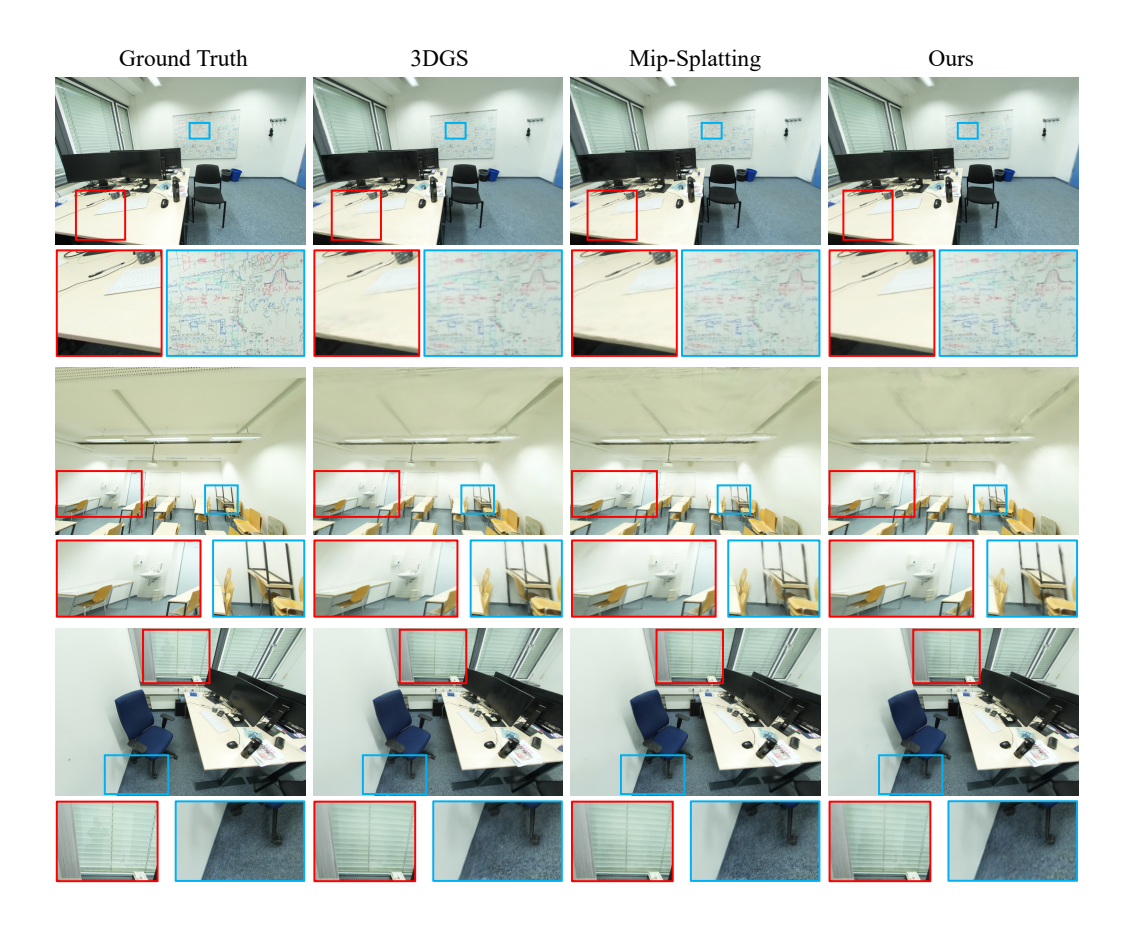


Figure 4: Qualitative Results on test views from ScanNet++ v2 scenes [29].

# 4.1 Reconstruction Quality

We measure reconstruction quality using the standard image metrics PSNR, SSIM and LPIPS. On the ScanNet++ dataset, our method consistently achieves scores close to both 3DGS and Mip-Splatting

despite using significantly fewer primitives, as visible in Table 1. We also compare against GS-MCMC [14], which allows precise limitations to the primitive population, and find that our results remain comparable, albeit slightly worse. For Mip-NeRF 360 scenes, we see a similar trend of comparable performance but with a more compact representation, as can be seen in Table 2. These results align with other works that suggest that the number of used Gaussians can be drastically reduced without a negative impact on performance through introduction of more advanced population control paradigms [8, 9]. While our approach introduces fundamental changes, we deliberately preserve components not directly related to the primitives. As such, more advanced paradigms can be applied in our primitives in a similar manner.

Figure 4 illustrates that our method faithfully reconstructs many challenging regions while sometimes showing slightly lower overall fidelity. These outcomes stem, in part, from the bounded nature of our primitives, which enforce sharper, more "binary" decisions in underconstrained areas. In practice, this can lead to crisper reconstructions in reflective or transparent regions—such as glass or distant backgrounds—but can also result in more conspicuous edges on rarely observed surfaces like ceilings. Overall, we find our approach to work the best in smaller, more densely captured scenes, as it retains strong geometric and visual clarity without overly densifying frequently observed regions. Further results on Mip-NeRF 360 scenes can be seen in Appendix C.

Table 1: **Quantitative Results** on ScanNet++ v2 scenes [29]. We limit GS-MCMC to use as many primitives as our approach does on average. Our method generates results of comparable performance while using much fewer primitives than 3DGS and Mip-Splatting.

PSNR	39f36da05b	5a269ba6fe	dc263dfbf0	08bbbdcc3d	fb564c935d	Prim.
3DGS [13]	27.693	23.675	23.436	22.444	23.210	738k
Mip-Splatting [30]	27.728	23.636	23.454	22.570	23.221	977k
GS-MCMC [14]	27.902	23.787	23.782	23.657	23.371	255k
LinPrim (ours)	27.557	23.845	22.668	22.312	23.801	255k

Table 2: **Quantitative Results** on Mip-NeRF 360 scenes [2]. Our approach generates results comparable in performance while using fewer primitives.

	PSNR	SSIM	LPIPS	Primitives
Zip-NeRF [3]	28.54	0.828	0.189	
Instant-NGP [20]	25.68	0.705	0.302	
3DGS [13]	27.43	0.813	0.217	3.32M
Mip-Splatting [30]	27.79	0.827	0.203	4.17M
LinPrim (ours)	26.63	0.803	0.221	1.79M

# 4.2 Tetrahedra Evaluation

In Table 3, we evaluate our tetrahedron approach using the same datasets, parameter constraints, and optimization framework described previously. By simply swapping octahedra for tetrahedra, we demonstrate that our method generalizes well to polyhedra with different geometric constraints and can still produce photorealistic reconstructions. Quantitatively, our tetrahedron approach performs similarly to octahedra on the ScanNet++ scenes and struggles on Mip-NeRF 360, highlighting the benefits of the increased symmetry and stability inherent to our octahedra. Although our existing pipeline was designed primarily around octahedra, these results confirm that it is not narrowly tailored to one specific primitive type. Nonetheless, tetrahedra could likely benefit from specialized adaptive population control and projection techniques that fully consider their asymmetric geometry, potentially closing the performance gap on currently challenging scenes. For instance, tuning how we split tetrahedra could yield further gains in accuracy.

Notably, tetrahedra and octahedra both converge to similar final primitive counts. On average, we obtained 259k tetrahedra for ScanNet++ scenes and 2.20M for Mip-NeRF 360, matching the counts of octahedra used in our experiments reasonably well. This suggests that switching between these primitive types does not inherently impose a significant memory or computational overhead. Future

work on refining geometric constraints, feature parameterization, and splitting heuristics could unlock even better performance for tetrahedron-based approaches.

Table 3: **Comparison** of the performance of our Octahedron and Tetrahedron approaches on Scan-Net++ v2 [29] and Mip-NeRF 360 [2] scenes. Both approaches produce comparable results on Scan-Net++ scenes, but our Octahedron approach reaches higher reconstruction quality on Mip-NeRF 360 scenes.

	ScanNet++			Mip-NeRF 360		
	PSNR	SSIM	LPIPS	PSNR	SSIM	LPIPS
Octahedron	24.04	0.849	0.281	26.63	0.803	0.221
Tetrahedron	24.05	0.848	0.302	25.96	0.790	0.247

#### 4.3 Limitations

While our method demonstrates comparable results and is easily understood and modified, it is not without drawbacks. First, the bounded nature of our primitives can introduce hard edges in poorly observed regions, resulting in more "segment-like" artifacts under limited view coverage. In these regions, the ability of Gaussian kernels to smoothly transition into each other leads to more visually pleasing results, even if the reconstruction is not necessarily better. Second, the current population control processes are not as consistent as their Gaussian counterparts. While we did adapt the processes to our primitives, the underlying paradigms are not as suitable for our polyhedron primitives. More specifically, polyhedra could benefit from more specialized processes for placing newly split primitives and improved criteria for determining which areas should be densified. It would be especially interesting to explore enhancements to 3DGS that address the above issues, as such improvements could disproportionately benefit our polyhedron-based approaches.

**Broader Impact.** Our work provides a new approach to novel view synthesis, which extends the design space of 3D scene representations. It has the potential to improve the quality and performance of 3D reconstruction and downstream applications, benefiting research in graphics, vision, robotics, and related fields. We do not anticipate any adverse environmental, societal or ethical effects.

# 5 Conclusion

We have presented novel approaches to volumetric scene reconstruction that leverage linear primitives, specifically octahedra and tetrahedra. Our method relies on a compact set of shape parameters and optimizes both geometry and appearance in a fully differentiable manner. By leveraging the inherent symmetries of octahedra, we achieve stable, high-fidelity results while maintaining a low memory footprint. At the same time, our experiments with tetrahedra demonstrate that the approach generalizes to other triangle-based volumes, underscoring its flexibility. Despite employing fewer primitives, our method consistently achieves comparable performance across challenging datasets, confirming its viability for real-world applications. Additionally, the bounded nature of our primitives yields more pronounced structural decisions in some rarely observed regions, sometimes leading to crisper reconstructions.

Promising future work could focus on leveraging the inherent properties of our primitives. As a concrete example, their triangular faces closely resemble traditional meshes. Developing efficient and accurate methods to binarize primitive opacity [7] presents significant potential for directly optimizing mesh representations from images. Additionally, although the rendering enhancements introduced by EVER [17] require significant changes for Gaussian-based methods, our primitives inherently allow for easily finding intersections with homogeneous primitives, avoiding the need for ray-tracing and enabling exact blending without additional computational overhead. Finally, integrating more specialized or advanced population control mechanisms could significantly enhance performance by improving primitive density in optimized scenes.

To summarize, we hope our linear primitives open up new possibilities for representing scenes in NVS applications and foster the creation of novel scene representations.

**Acknowledgements.** This work was supported by the ERC Consolidator Grant Gen3D (101171131) and the German Research Foundation (DFG) Research Unit "Learning and Simulation in Visual Computing". We thank Angela Dai for the video voice-over.

# References

- [1] J. T. Barron, B. Mildenhall, M. Tancik, P. Hedman, R. Martin-Brualla, and P. P. Srinivasan. Mip-nerf: A multiscale representation for anti-aliasing neural radiance fields. In *Proceedings of the IEEE/CVF international conference on computer vision*, pages 5855–5864, 2021.
- [2] J. T. Barron, B. Mildenhall, D. Verbin, P. P. Srinivasan, and P. Hedman. Mip-nerf 360: Unbounded anti-aliased neural radiance fields. In *Proceedings of the IEEE/CVF conference on computer vision and pattern recognition*, pages 5470–5479, 2022.
- [3] J. T. Barron, B. Mildenhall, D. Verbin, P. P. Srinivasan, and P. Hedman. Zip-NeRF: Anti-Aliased Grid-Based Neural Radiance Fields, Oct. 2023. arXiv:2304.06706.
- [4] H. Chen, R. Chen, Q. Qu, Z. Wang, T. Liu, X. Chen, and Y. Y. Chung. Beyond Gaussians: Fast and High-Fidelity 3D Splatting with Linear Kernels, Nov. 2024. arXiv:2411.12440.
- [5] Y. Chen, Z. Chen, C. Zhang, F. Wang, X. Yang, Y. Wang, Z. Cai, L. Yang, H. Liu, and G. Lin. Gaussianeditor: Swift and controllable 3d editing with gaussian splatting. In *Proceedings of the IEEE/CVF conference on computer vision and pattern recognition*, pages 21476–21485, 2024.
- [6] Y. Chen, Y. Nie, B. Ummenhofer, R. Birkl, M. Paulitsch, M. Müller, and M. Nießner. Mesh2NeRF: Direct Mesh Supervision for Neural Radiance Field Representation and Generation. In A. Leonardis, E. Ricci, S. Roth, O. Russakovsky, T. Sattler, and G. Varol, editors, Computer Vision – ECCV 2024, volume 15067, pages 173–191. Springer Nature Switzerland, Cham, 2025. Series Title: Lecture Notes in Computer Science.
- [7] Z. Chen, T. Funkhouser, P. Hedman, and A. Tagliasacchi. Mobilenerf: Exploiting the polygon rasterization pipeline for efficient neural field rendering on mobile architectures. In *Proceedings of the IEEE/CVF* Conference on Computer Vision and Pattern Recognition, pages 16569–16578, 2023.
- [8] G. Fang and B. Wang. Mini-Splatting: Representing Scenes with a Constrained Number of Gaussians. In A. Leonardis, E. Ricci, S. Roth, O. Russakovsky, T. Sattler, and G. Varol, editors, *Computer Vision – ECCV 2024*, volume 15135, pages 165–181. Springer Nature Switzerland, Cham, 2024. Series Title: Lecture Notes in Computer Science.
- [9] G. Fang and B. Wang. Mini-Splatting2: Building 360 Scenes within Minutes via Aggressive Gaussian Densification, Nov. 2024. arXiv:2411.12788 [cs].
- [10] M. Gross and H. Pfister. Point-based graphics. Elsevier, 2011.
- [11] J. Held, R. Vandeghen, A. Hamdi, A. Deliege, A. Cioppa, S. Giancola, A. Vedaldi, B. Ghanem, and M. V. Droogenbroeck. 3D Convex Splatting: Radiance Field Rendering with 3D Smooth Convexes, Nov. 2024. arXiv:2411.14974.
- [12] B. Huang, Z. Yu, A. Chen, A. Geiger, and S. Gao. 2D Gaussian Splatting for Geometrically Accurate Radiance Fields. In *Special Interest Group on Computer Graphics and Interactive Techniques Conference Conference Papers* '24, pages 1–11, Denver CO USA, July 2024. ACM.
- [13] B. Kerbl, G. Kopanas, T. Leimkühler, and G. Drettakis. 3D Gaussian Splatting for Real-Time Radiance Field Rendering, Aug. 2023. arXiv:2308.04079.
- [14] S. Kheradmand, D. Rebain, G. Sharma, W. Sun, J. Tseng, H. Isack, A. Kar, A. Tagliasacchi, and K. M. Yi. 3D Gaussian Splatting as Markov Chain Monte Carlo, June 2024. arXiv:2404.09591.
- [15] D. P. Kingma and J. Ba. Adam: A Method for Stochastic Optimization, Jan. 2017. arXiv:1412.6980.
- [16] G. Kopanas, J. Philip, T. Leimkühler, and G. Drettakis. Point-Based Neural Rendering with Per-View Optimization. Computer Graphics Forum, 40(4):29–43, July 2021.
- [17] A. Mai, P. Hedman, G. Kopanas, D. Verbin, D. Futschik, Q. Xu, F. Kuester, J. T. Barron, and Y. Zhang. EVER: Exact Volumetric Ellipsoid Rendering for Real-time View Synthesis, Oct. 2024. arXiv:2410.01804.
- [18] B. Mildenhall, P. P. Srinivasan, M. Tancik, J. T. Barron, R. Ramamoorthi, and R. Ng. NeRF: representing scenes as neural radiance fields for view synthesis. *Communications of the ACM*, 65(1):99–106, Jan. 2022.
- [19] T. Möller and B. Trumbore. Fast, minimum storage ray/triangle intersection. In ACM SIGGRAPH 2005 Courses, SIGGRAPH '05, pages 7-es, New York, NY, USA, July 2005. Association for Computing Machinery.
- [20] T. Müller, A. Evans, C. Schied, and A. Keller. Instant neural graphics primitives with a multiresolution hash encoding. *ACM Transactions on Graphics*, 41(4):1–15, July 2022.

- [21] M. Niemeyer, L. Mescheder, M. Oechsle, and A. Geiger. Differentiable volumetric rendering: Learning implicit 3d representations without 3d supervision. In *Proceedings of the IEEE/CVF conference on computer vision and pattern recognition*, pages 3504–3515, 2020.
- [22] A. Pumarola, E. Corona, G. Pons-Moll, and F. Moreno-Noguer. D-NeRF: Neural Radiance Fields for Dynamic Scenes, Nov. 2020. arXiv:2011.13961 [cs].
- [23] D. Rückert, L. Franke, and M. Stamminger. ADOP: approximate differentiable one-pixel point rendering. ACM Transactions on Graphics, 41(4):1–14, July 2022.
- [24] J. L. Schonberger and J.-M. Frahm. Structure-from-motion revisited. In Proceedings of the IEEE conference on computer vision and pattern recognition, pages 4104–4113, 2016.
- [25] J. Tang, J. Ren, H. Zhou, Z. Liu, and G. Zeng. DreamGaussian: Generative Gaussian Splatting for Efficient 3D Content Creation, Mar. 2024. arXiv:2309.16653.
- [26] J. Tang, H. Zhou, X. Chen, T. Hu, E. Ding, J. Wang, and G. Zeng. Delicate Textured Mesh Recovery from NeRF via Adaptive Surface Refinement, Aug. 2023. arXiv:2303.02091 [cs].
- [27] P. Wang, L. Liu, Y. Liu, C. Theobalt, T. Komura, and W. Wang. NeuS: Learning Neural Implicit Surfaces by Volume Rendering for Multi-view Reconstruction, Feb. 2023. arXiv:2106.10689 [cs].
- [28] Q. Xu, Z. Xu, J. Philip, S. Bi, Z. Shu, K. Sunkavalli, and U. Neumann. Point-nerf: Point-based neural radiance fields. In *Proceedings of the IEEE/CVF conference on computer vision and pattern recognition*, pages 5438–5448, 2022.
- [29] C. Yeshwanth, Y.-C. Liu, M. Nießner, and A. Dai. Scannet++: A high-fidelity dataset of 3d indoor scenes. In *Proceedings of the IEEE/CVF International Conference on Computer Vision*, pages 12–22, 2023.
- [30] Z. Yu, A. Chen, B. Huang, T. Sattler, and A. Geiger. Mip-splatting: Alias-free 3d gaussian splatting. In Proceedings of the IEEE/CVF Conference on Computer Vision and Pattern Recognition, pages 19447– 19456, 2024.
- [31] Y.-J. Yuan, Y.-T. Sun, Y.-K. Lai, Y. Ma, R. Jia, and L. Gao. NeRF-Editing: Geometry Editing of Neural Radiance Fields, May 2022. arXiv:2205.04978 [cs].
- [32] M. Zwicker, H. Pfister, J. Van Baar, and M. Gross. EWA volume splatting. In *Proceedings Visualization*, 2001. VIS'01., pages 29–538. IEEE, 2001.
- [33] M. Zwicker, H. Pfister, J. van Baar, and M. Gross. EWA splatting. IEEE Transactions on Visualization and Computer Graphics, 8(3):223–238, July 2002. Conference Name: IEEE Transactions on Visualization and Computer Graphics.

# A Rendering Speed

We evaluate the rendering speed of our methods by measuring the average time required to render every train and test view for each scene. All timings are recorded on a single RTX 3090 GPU at the same resolutions used for optimization, ensuring a fair comparison across all methods.

As shown in Table 4, all evaluated approaches achieve real-time performance, demonstrating that our primitives can be rendered interactively. Our octahedron-based method reaches 68fps on ScanNet++ and 29fps on Mip-NeRF 360. Meanwhile, our tetrahedron variant achieves 175fps on ScanNet++ and 66fps on Mip-NeRF 360, making it about twice as fast as the octahedron approach due to having only half the faces to process per primitive.

These results confirm that the majority of the rendering cost stems from iterating over

Table 4: **Quantitative Results** on the rendering speed of tested approaches. We report the average time to render every train and test view on ScanNet++ v2 and Mip-NeRF 360 scenes.

	ScanNet++	Mip-NeRF 360
3DGS [13]	5.7ms	8.8ms
Mip-Splatting [30]	11.0ms	20.3ms
Octahedron (ours)	14.6ms	34.6ms
Tetrahedron (ours)	5.7ms	15.2ms

each face of each primitive to compute ray intersections. Since tetrahedra contain fewer faces, each pass requires less computational effort, thereby boosting the frame rate substantially.

While our methods consistently demonstrate real-time rendering across both datasets, we must consider that the difference in primitive count can impact performance. Nevertheless, these experiments underscore the capability of our linear primitives, whether octahedra or tetrahedra, to balance high-fidelity reconstruction with the interactivity needed for real-time applications.

# **B** Anti-Aliasing

Table 5 presents the effect of our antialiasing filters on reconstruction quality for one Mip-NeRF 360 and one ScanNet++ scene. We observe that enabling each filter individually improves quantitative performance, most prominently in PSNR. Combining both filters yields an even larger gain, indicating their complementary nature. Interestingly, LPIPS shows virtually no changes, suggesting that while our filters enhance pixel-level similarity, high-level perceptual features remain relatively stable. Neither filter significantly affects the number of primitives used in the reconstruction process, which indicates that these techniques refine visual fidelity without complicating the underlying geometry or increasing memory overhead. Overall, our results demonstrate that applying these filters leads to visually cleaner outputs and higher numerical scores, reinforcing the value of antialiasing.

Table 5: **Ablation** showing the impact of the two filters used in our anti-aliasing efforts. Combining both filters reduces the reconstruction error.

Filt	ters	Bonsai		dc263dfbf0			
2D	3D	PSNR	SSIM	LPIPS	PSNR	SSIM	LPIPS
		30.84	0.929	0.196	22.46	0.870	0.267
$\checkmark$		30.96	0.931	0.196	22.59	0.870	0.266
	$\checkmark$	30.97	0.930	0.195	22.66	0.871	0.266
$\checkmark$	$\checkmark$	31.21	0.936	0.195	22.67	0.871	0.266

#### C Additional Results

In Figure 5 we show qualitative results of our representation on Mip-NeRF 360 scenes. In Table 6 we show the average PSNR, SSIM, and LPIPS metrics on the used ScanNet++ v2 scenes.

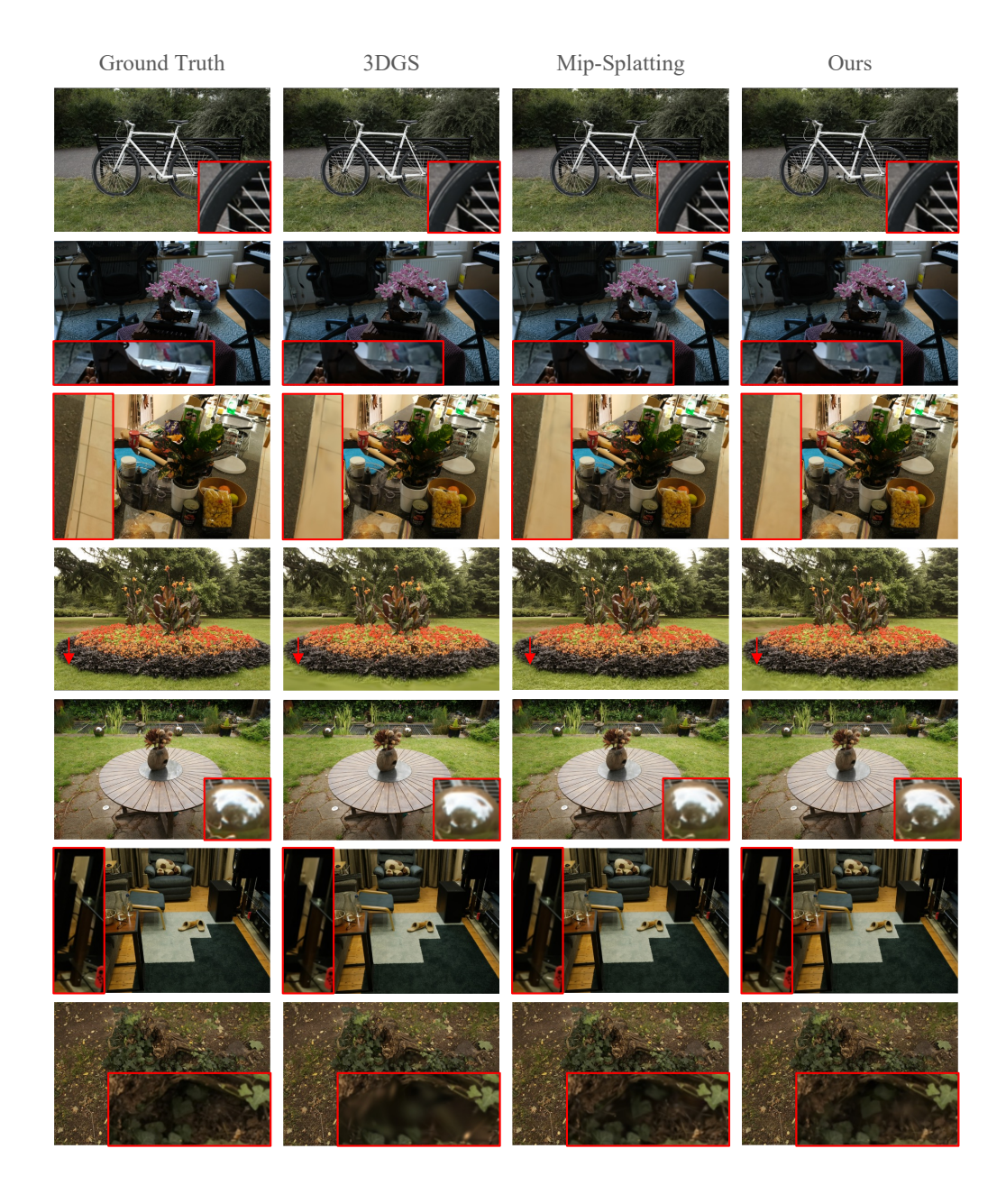


Figure 5: Qualitative Results on test views from Mip-NeRF 360 scenes [2].

Table 6: **Quantitative Results** on ScanNet++ v2 scenes [29]. We limit GS-MCMC to use as many primitives as our approach does on average. Presented results are the average over the five scenes considered during our evaluation.

PSNR	PSNR	SSIM	LPIPS	Primitives
3DGS [13]	24.092	0.853	0.263	738k
Mip-Splatting [30] GS-MCMC [14]	24.122	0.852	0.261	977k
GS-MCMC [14]	24.500	0.862	0.256	255k
LinPrim (ours)	24.037	0.849	0.281	255k